

## Disaggregation bands as an indicator for slow creep activity on blind faults

Christian Brandes<sup>1✉</sup>, David C. Tanner<sup>2</sup>, Haakon Fossen<sup>3</sup>, Matthias Halisch<sup>2</sup> & Katharina Müller<sup>1</sup>

Hidden, blind faults have a strong seismic hazard potential. Consequently, there is a great demand for a robust geological indicator of neotectonic activity on such faults. Here, we conduct field measurements of disaggregation bands above known underlying blind faults at several locations in Central Europe. We observe that the disaggregation bands have the same orientation as that of the faults, indicating their close connection. Disaggregation bands develop in unconsolidated, near-surface, sandy sediments. They form by shear-related reorganization of the sediment fabric, as a consequence of grain rolling and sliding processes, which can reduce the porosity. Using an analogue shearing experiment, we show that disaggregation bands can form at a velocity of  $2 \text{ cm h}^{-1}$ , which is several orders of magnitude slower than seismogenic fault-slip velocities. Based on the field data and the experiments, we infer that disaggregation bands can form in the process zone of active blind faults and serve as an indicator of neotectonic activity, even if the fault creeps at very low slip velocity. Disaggregation bands could open a new path to detect hidden active faults undergoing aseismic movements.

<sup>1</sup>Institut für Geologie, Gottfried Wilhelm Leibniz Universität Hannover, Callinstr. 30, 30167 Hannover, Germany. <sup>2</sup>Leibniz Institute for Applied Geophysics (LIAG), Stilleweg 2, 30655 Hannover, Germany. <sup>3</sup>Natural History Collections, University Museum of Bergen, University of Bergen, PO Box 7803, 5020 Bergen, Norway. ✉email: [brandes@geowi.uni-hannover.de](mailto:brandes@geowi.uni-hannover.de)

**B**lind faults, that is, hidden subsurface faults that do not rupture the surface and often covered by unconsolidated sediments, can be the source of unexpected, damaging, and fatal earthquakes that represent a major seismic hazard in urban areas<sup>1</sup>. Detecting active blind faults is therefore highly relevant to assess the seismic hazard of a region, but this remains a challenge, especially in areas where there are long intervals between individual earthquakes. Paleoseismological studies often rely on soft-sediment deformation structures, such as sand-volcanoes, to identify past seismic events, e.g.,<sup>2,3</sup>. However, these structures can also form due to non-tectonic drivers, such as water discharge<sup>4</sup> or permafrost<sup>5</sup>. Consequently, soft-sediment deformation structures are ambiguous.

Slip rates on active faults vary over many orders of magnitude, ranging from  $\text{m min}^{-1}$  for seismic ruptures<sup>6</sup> over  $\text{cm d}^{-1}$  for slow slip/creep events<sup>7</sup> to  $\text{cm yr}^{-1}$  for continuous creep, e.g.,<sup>8</sup>. In a typical seismic cycle, an extremely short co-seismic interval may be followed by a long period of post-seismic creep<sup>9</sup>. At present, fault activity is regarded as a continuum between the former and latter<sup>10</sup>. Accordingly, hazard assessment based on only seismic events ignores a large part of the fault activity. In addition, fault creep is difficult to derive from the geological record<sup>11</sup>. Structures such as sand-volcanoes, slump structures, seismites and clastic dykes can form co-seismically due to groundwater expulsion but fail to indicate aseismic creep. To the best of our knowledge, there is no simple method to infer aseismic creep on blind faults from geological structures in overlying sediments. However, because a creeping fault may return to rupture mode in the future, or have interseismic periods that exceed the length of instrumentally recorded seismicity, there is strong demand for a universal geological indicator of blind fault activity that is sensitive to movement below seismogenic displacement velocities (i.e., creeping or slow slip). This indicator is required for a profound hazard risk evaluation.

In general, deformation bands are planar structural elements that develop in porous sand and sandstones in the upper crust, e.g.,<sup>12,13</sup>. They can be further subdivided into cataclastic and non-cataclastic bands, the latter also known as disaggregation bands. In the former, cataclasis occurs that leads to grain-size reduction and thus porosity reduction in the band<sup>14,15</sup>. On the contrary, the latter preferentially form at the near-surface in unconsolidated or weakly-consolidated sandy sediments by grain rolling and sliding processes, i.e., particulate or granular flow<sup>16</sup>.

Based on datasets from the San Andreas Fault, it has been shown that cataclastic deformation bands, while absent in creeping fault segments, are present in sediments overlying active, seismogenically-rupturing fault segments<sup>17</sup>. The authors argue that cataclastic deformation bands are therefore suitable indicators of co-seismic slip. Similarly, cataclastic bands were observed in the vicinity of actively-rupturing faults in the upper Rhine Graben in Germany<sup>18</sup>. Cataclastic deformation band formation in near-surface sediments is interpreted to involve force-chains and grain-bridge processes<sup>17</sup>, where bridge failure is associated with grain comminution and flaking<sup>19</sup>. Experimental studies on deformation bands in both sandstones and unlithified sand have been carried out<sup>20,21</sup>.

In the following, we assess the hypothesis that non-cataclastic disaggregation bands can form during slow slip (creep events) on underlying faults. Based on field data, we describe their structural characteristics and use physical experiments to reproduce them in the laboratory.

## Results

**Disaggregation bands in nature.** Excellent examples of disaggregation shear bands can be observed in outcrops above blind

faults in northern Germany and northern Denmark (Fig. 1). The faults in Denmark (Fig. 1a, b) were seismically active in the Lateglacial<sup>22</sup> and there has been recent seismicity in this area, as instrumentally recorded since 1930<sup>23</sup>. At the Aller Fault in northern Germany (Fig. 1a), potential neotectonic fault activity is documented by longitudinal river profiles, c.f.<sup>24</sup> and historic earthquakes, c.f.<sup>25</sup>. Disaggregation bands are developed in sandy Pleistocene sediments, have displacements ranging from centimetres to decimetres, and often form conjugate networks or en-échelon stepping arrays with intervals between individual bands that range from centimetres to metres. Most importantly, their strike closely matches that of known blind faults in the subsurface. In some locations, the bands show an orthogonal pattern in map view that reflects the geometry of an underlying pull-apart structure<sup>26</sup>.

Most of the bands show normal shear offsets (Fig. 1b–d), indicating normal dip-slip movement in the subsurface. The bands were observed at depths down to 17 m. We exclude compaction and differential compaction as driving mechanisms for shear-band formation, because outcrops in the region, in which similar sediments are exposed, do not show any evidence for deformation bands. All bands shown in this study have been interpreted to reflect Pleistocene fault movement<sup>22,26</sup>.

Deformation bands exposed near Freden in northern Germany (Fig. 1d) are good examples of non-cataclastic, near surface, disaggregation shear-bands that developed in sandy, ice-marginal, delta-slope Pleistocene sediments<sup>27</sup>. Sieve analysis shows the host material is a medium sand (mean grain size  $460 \pm 150(1\sigma) \mu\text{m}$  ( $1.3 \pm 0.6(1\sigma) \phi$ )), moderately well sorted, very fine skewed). The disaggregation bands have thicknesses of 0.1–4.0 cm (Fig. 2a), dip angles of  $55^\circ$ – $75^\circ$ , and a consistent normal sense of displacement. We observe a positive increase in thickness with displacement and the thickness distribution follows a strict negative power law (Fig. 2b).

Thin-sections display distinct pore-space reduction within the analysed bands (in Fig. 1e, 37% in the host material, 25% in the band). However, not all bands show a porosity reduction. The grains are not fractured and grain-size reduction did not take place, meaning that cataclasis did not occur (Fig. 1e). This is also supported by the similar distribution of grain-size inside and outside of the disaggregation band in thin section (Fig. 3). To support the thin-section analysis, we also carried out  $\mu$ -CT measurements, which confirms the strong porosity loss within the natural disaggregation bands. Some analysed disaggregation bands show a clear alignment of elongated grains, in which the boundary between the band and the host sediment can be very distinct (Fig. 3). Texture analysis shows that the grains outside the band are near-randomly orientated, while the grains in the band have a strong preferred grain texture, especially for those grains with a high aspect ratio (Fig. 3). A comparable observation of grain-axis alignment was shown for the near-surface disaggregation bands in the Børglum fault area (Fig. 1a)<sup>28</sup>.

**Disaggregation bands in experiments.** To test the hypothesis that disaggregation shear-band formation is associated with slip at subseismogenic velocities, we performed a series of physical analogue experiments (Fig. 4), using the material from the outcrop shown in Fig. 1d. The experiments were designed to analyse the influence of the rate of slip, rather than the mode of slip. The applied shear velocities (corresponding to a bulk strain rate of  $5.6$ – $11 \cdot 10^{-4} \text{s}^{-1}$ ) at a model velocity of  $2 \text{cm h}^{-1}$ , are in the range of slow slip/creep events, cf.<sup>29</sup>, i.e. several orders of magnitude lower than typical seismogenic displacement velocities, e.g.,<sup>6,30</sup>. During our experiments, a disaggregation band formed in the centre of the shear-box, where a velocity discontinuity

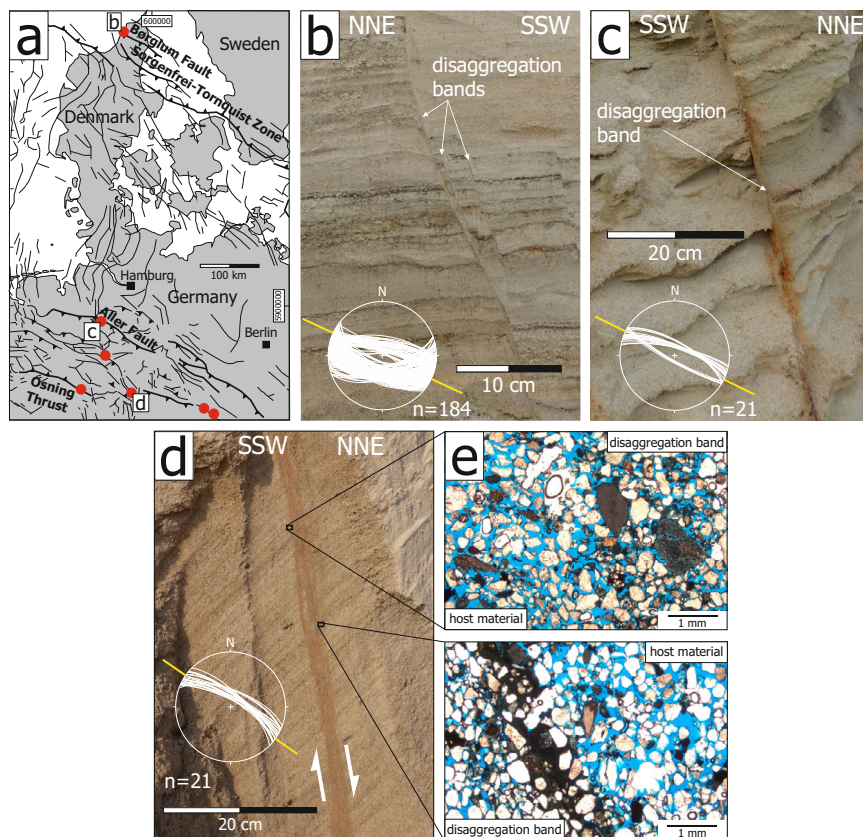


**Fig. 1** Field examples of disaggregation bands developed in sandy sediments in the vicinity of blind faults. Each stereographic projection (lower hemisphere, equal area) shows the strike of the blind fault in yellow; the great circles represent the orientation of the disaggregation bands measured in the overlying sediments. **a** Fault map of Central Europe, modified after<sup>58</sup>. Red dots indicate outcrops of disaggregation bands in northern Europe, data this work and<sup>59</sup>. **b** Børglum Fault (northern boundary fault of the Sorgenfrei-Tornquist Zone, northern Denmark). **c** Aller Fault, northern Germany. **d** Freden site, northern Germany. **e** Thin-section photographs of a disaggregation band and host material from **d**. Note the low pore-space within the band.

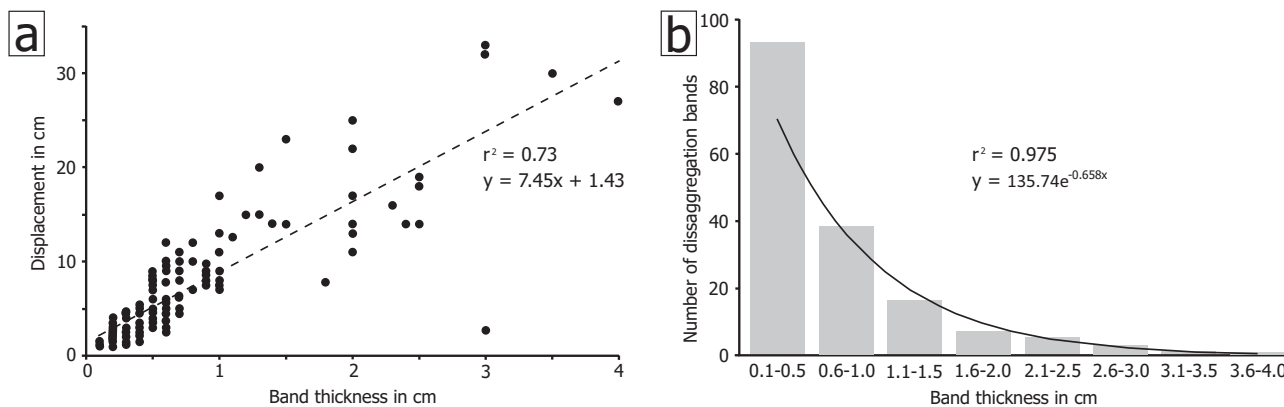


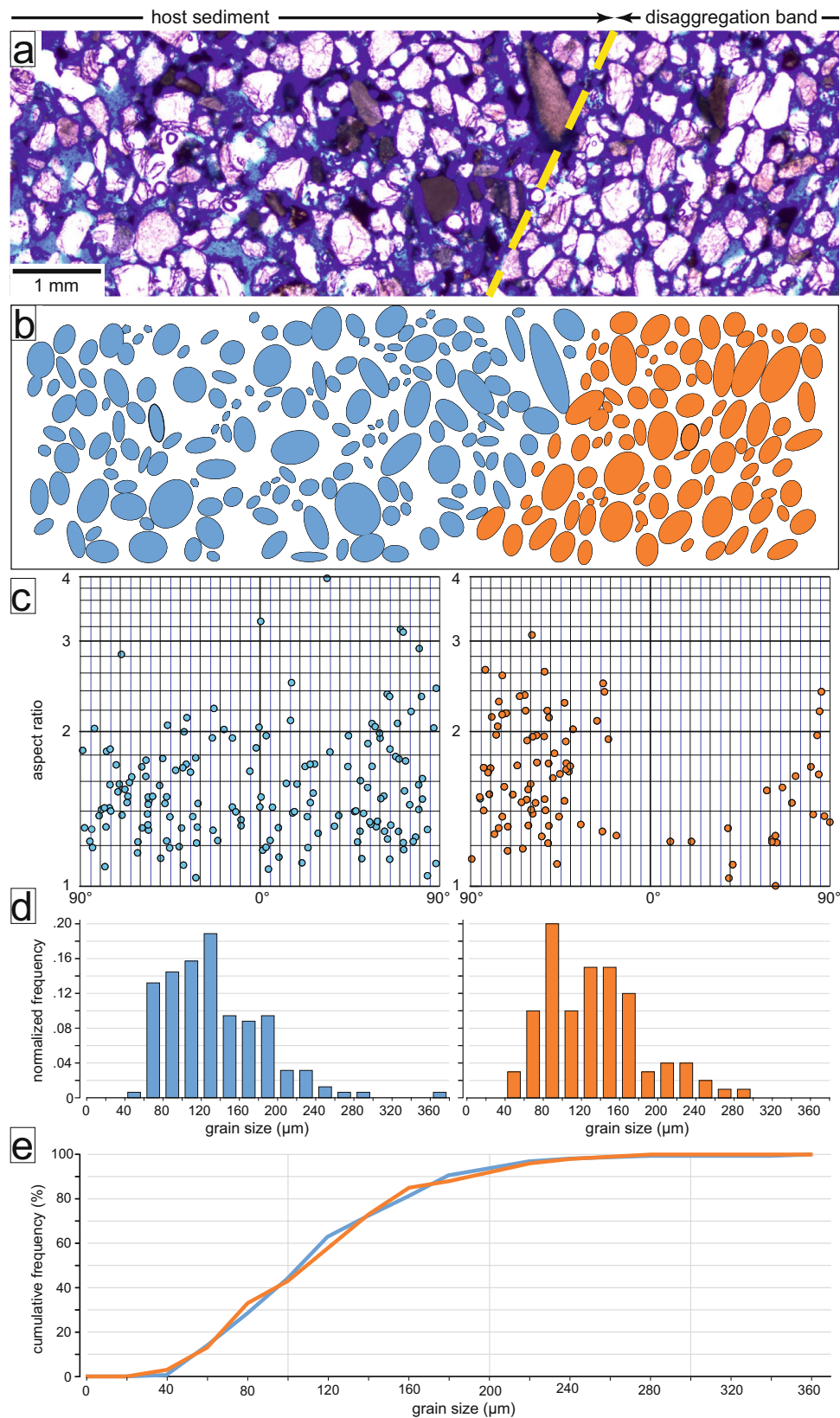
**Fig. 2** Field data of 155 disaggregation bands exposed in the Freden outcrop. **a** Thickness/displacement relationship; band thickness shows a linear relationship to displacement. **b** Thickness/frequency of disaggregation bands, showing a power-law distribution. The disaggregation bands have a median thickness of 0.2 cm.

occurs between the stationary and the moving halves of the shear-box (Fig. 4a). The limitations of the experiments are the lack of confining pressure and pore-fluids, the fact that the sediments are not deposited by natural processes, that we could not carry out long-term deformation (i.e. over a year) and that the experiment contains only a small volume and is open on one side. However, results of experiments using the same set-up are robust<sup>32</sup>. After the experiments, the shear band was conserved in resin to allow detailed study of textural changes in thin section. In experiments

a distinct disaggregation band developed, without the involvement of cataclastic processes (Figs. 1b and 5).

We conducted experiments (fifteen in total) at two different velocities (2 cm h<sup>-1</sup> and 3600 cm h<sup>-1</sup>) to represent fault creep and fault rupture speeds, respectively.

The experimental disaggregation bands are tabular structural elements (Fig. 5), with a thickness of up to 5–9 mm after 6 cm of displacement, independent of the model velocity. Similar to the natural bands, a loss in porosity can be observed from the host



material to the band in thin sections (Fig. 4b). Additional X-ray micro-computed tomography ( $\mu$ -CT) measurements and digital image analysis (DIA) therefrom confirm porosity loss within both the natural and experimental disaggregation bands (Fig. 6a, natural band; 32–41% in the host material, 24–34% in the band; Fig. 6b, experimental band; 20.5–21.5% in the host material,

19.5–20.5% in the band). The porosity loss in the experimental bands is much lower compared to natural bands, indeed not every experiment showed a clear porosity loss. This is probably caused by the lack of confining pressure. Nevertheless, with our experiments, we are able to reproduce the major characteristics of natural disaggregation bands (Fig. 5).

**Fig. 3 Texture analysis of a disaggregation band and its host.** **a** Photomicrograph of a disaggregation band in sand from the Freden site. Blue colour is due to the resin that was used to fix the grains. Dashed line represents the boundary of the disaggregation band to the right. **b** Best-fit ellipses calculated from the digitised grain outlines, using the software EllipseFit<sup>60</sup>. Blue --- grains outside of band ( $n = 163$ ), orange --- grains with the band ( $n = 104$ ). **c** Aspect ratio of the grains against their long axis orientation (left (blue) --- outside of the band, right (orange) --- inside the band). Reference direction ( $0^\circ$ ) is horizontal. Clearly, the orientation of grains outside of the band have no preferred orientation, while the grains in the band have a strong preferred grain texture, especially for grains with a high aspect ratio. **d** Histograms of normalised frequency against grain size, (left (blue) --- outside of the band, right (orange) --- inside the band). Note the similar distribution, which shows there is no grain-size reduction in the disaggregation band. **e** Cumulative frequency against grain-size (blue --- outside of the band, orange --- inside the band).

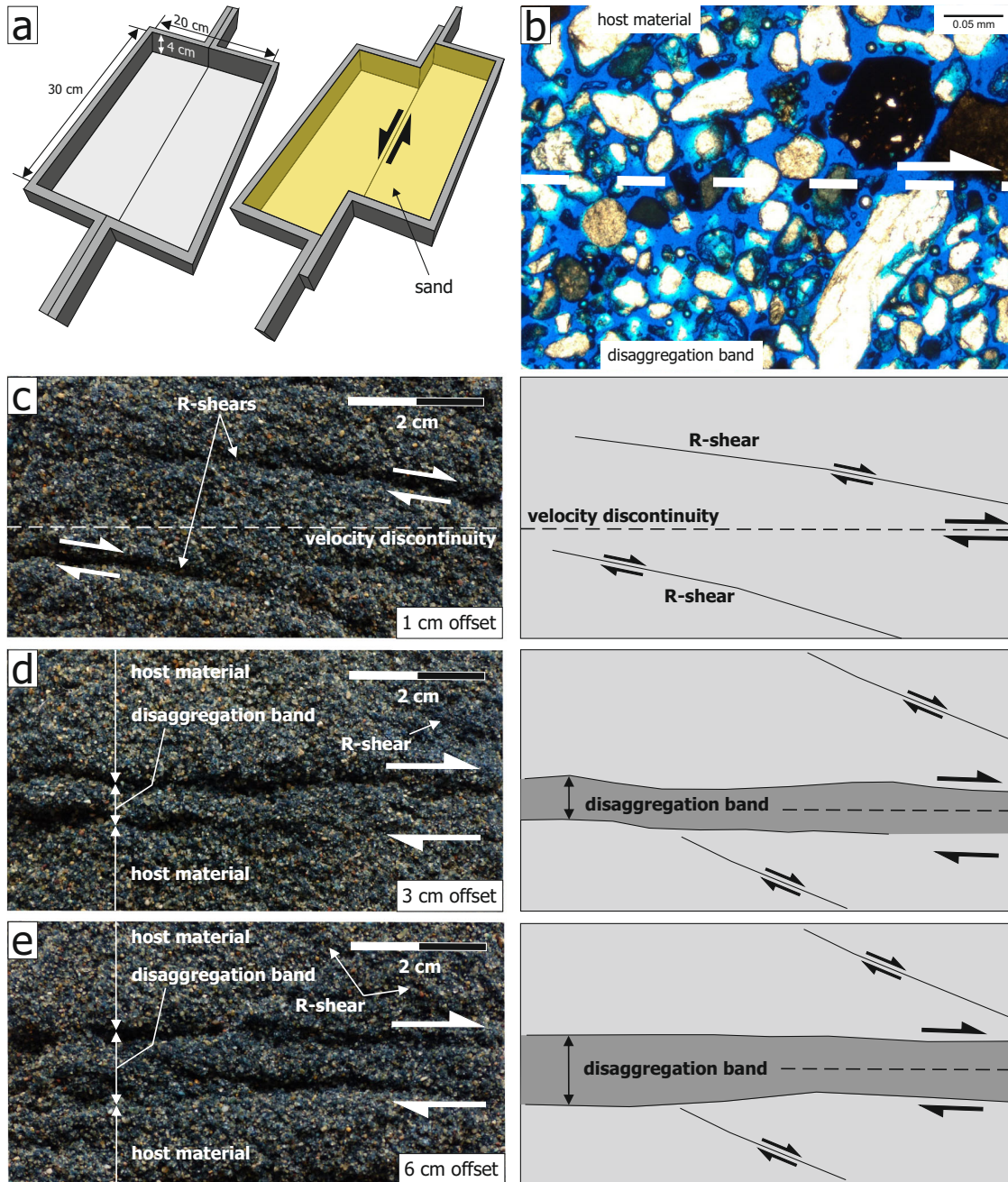


**Fig. 4 Experimental results.** **a** Experimental set-up of the shear box. The box is filled with natural material from the Freden outcrop. **b** Thin section of an experimental disaggregation band. Note the difference in porosity from the host material to the band. **c** After 1 cm of offset, Riedel shears (R-shears) evolve near to the velocity discontinuity. **d** After 3 cm offset, a central disaggregation band develops and the R-shears become inactive. **e** After 6 cm offset, the band becomes more distinct and grows thicker. The dark areas are grooves in the sample that result from the hindered resin percolation due to changes in porosity.

Most creeping faults show distinct creep events in which they achieve most of their displacement, e.g.,<sup>31</sup>, therefore the short duration of the experiments of several hours does not affect the comparability to the natural disaggregation bands. The design of the experiment with the strike-slip set-up makes it prone to the formation of Riedel shears. The formation of the main shear zone in the experiments results from the interlinkage of anastomosing Riedel P- and Y-shears<sup>32</sup>. The complete development of different structural elements indicates that the limited size of the experimental set-up is sufficient. Locally, small pop-up structures can develop, but most of the main shear zone remains undisturbed and is suitable for analysis<sup>32</sup>. We also observe Riedel shears that develop in the initial phase at a low angle to the main shear discontinuity (Fig. 4c), as well as occasionally local pop-up structures. After increased displacement, deformation localizes on the central shear band above the velocity discontinuity in the centre of the shear box (Fig. 4d–e). A similar observation was made in other experiments<sup>33</sup>. They show that shear zone development starts with a diffuse sigmoidal patch and subsequently curved shear zones develop that finally connect and form the main shear zone. We speculate that this is also possibly how natural disaggregation bands in sands evolve and the common branching and merging of the bands might be caused by these

Riedel shears. However, this is only a minor point; our main conclusion is the velocity independence of the disaggregation band formation and their potential as indicators for non-rupturing blind fault activity.

In summary, our shear-box experiments, carried out at shear velocities typical for aseismic creep, produced disaggregation bands in sand that closely match natural examples observed in the field, imply that natural disaggregation bands are an indicator of active slip on sediment-covered subsurface faults. The fact that they can be reproduced in a simple experiment underlines their universal manifestation, independent of the geological setting.

## Discussion

Our field observations imply that disaggregation bands (i.e., non-cataclastic deformation bands) frequently occur above blind faults in northern Germany and northern Denmark (Fig. 1). As the analysed disaggregation bands can show a very distinct pore-space reduction, we interpret their formation as the consequence of fabric reorganization by granular flow (Fig. 3). A suitable mechanical model to explain shear-band evolution in granular material is the Thomas-Hill-Mandel shear-band model<sup>34</sup>. Shear-band formation is an equilibrium bifurcation from a homogeneous deformation<sup>34</sup>. During this process, the material properties bifurcate into the less-deformed host material and the deformation band<sup>35</sup>. Shear-band formation in sand is regarded as a plastic volume change known as Reynold's effect, e.g.,<sup>36</sup>, often leading to dilation in the band, e.g.<sup>37</sup>, and resulting strain softening. However, for granular material, especially if it consists of anisotropic particles, the realignment of particles allows for denser packing<sup>38</sup>, as observed in both the natural and the experimental disaggregation bands described in this study. In the field, we observe systematic increase in the thickness of disaggregation bands with increasing displacement (Fig. 2a) and a loss of porosity (Figs. 1e and 3). We propose that the loss of porosity leads to increased grain contact area, which leads to strain hardening. The band responds by laterally thickening.

During shearing, the grains are reorganised, with a preferred orientation of long axes of the grains (parallel to the band boundary in Fig. 3), as was also observed in experiments by<sup>39</sup>. In their work, grain column buckling occurs that causes initial strain hardening followed by strain softening and void formation within the shear bands. From our study of thin-sections of disaggregation bands from the Freden outcrop, we conclude that grain reorientation took place that lead to a denser packing and potential locking of grains (Fig. 1e). However, we do not observe systematic voids in the shear bands. Because of grain locking,

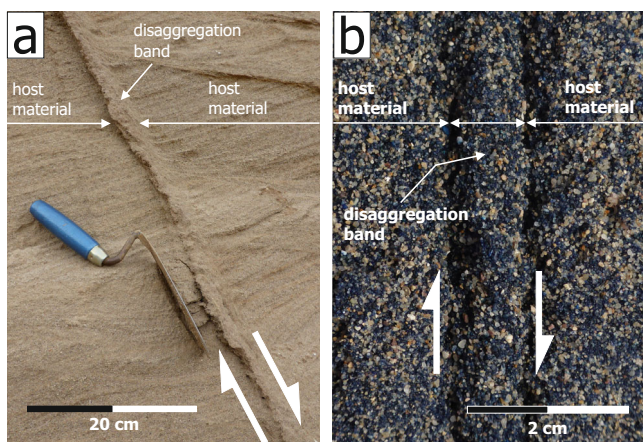


**Fig. 5 Comparison of natural and experiment disaggregation bands.** **a** Natural disaggregation band in the Freden outcrop. **b** Experimental disaggregation band after 6 cm offset with a shear velocity of  $2 \text{ cm h}^{-1}$ , cut at 1 cm below the upper surface of the sheared sand package.

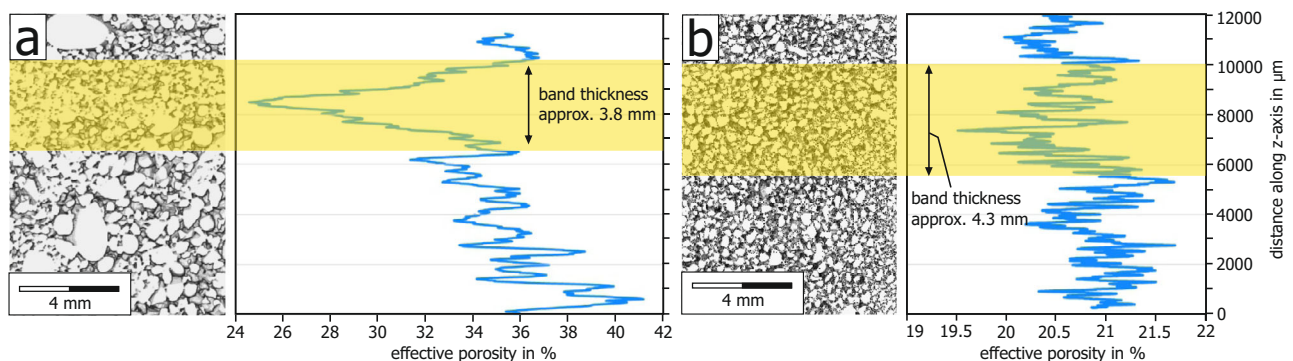


**Fig. 6  $\mu$ -CT analysis of disaggregation bands.** **a** Natural band from the Freden outcrop (see Fig. 1 for location). The  $\mu$ -CT analysis indicates a strong decrease in porosity within the band. **b**  $\mu$ -CT analysis of an experimental disaggregation band. A porosity reduction also occurs across this band, but is much less pronounced than in the natural example. The porosity loss in both cases is the result of the shear-induced grain-fabric reorganization. The lower loss in porosity in case of the experimental band is likely due to the lack of a confining pressure. The  $\mu$ -CT results support the thin-section analysis.

progressive strain hardening can only occur during deformation; the bands thicken and thus grow into their characteristic tabular shape. Because of the positive increase in band thickness with displacement, and the thickness distribution that follows a strict negative power law (Fig. 2), we postulate that all disaggregation bands began with a small (ca. 1 mm) thickness. Further increments of displacement increased the band's width (i.e., effectively work hardening), but ongoing deformation was accrued on increasingly less bands to produce the power-law distribution that we observe. In the study by<sup>21</sup>, experimental deformation bands were produced under low strain rates in Permian Locharbriggs sandstone. These authors conclude that increasing the amount of strain would lead to wider bands, but they do not observe post-failure strain hardening. Therefore their study is only partly compatible with our analyses, as we use unconsolidated sand, and cataclasis did not take place in our bands. Instead, we observe that the deformation was exclusively compensated for by reorganisation of the grain fabric (Fig. 3).

The thickness of the disaggregation bands observed in the Freden outcrop (Fig. 2) ranges from 0.1–4.0 cm, but most of the bands are 0.1–1.0 cm thick, with a median thickness of 0.2 cm (Fig. 2). This is in good agreement with<sup>40</sup> who suggest that shear bands in granular material have a thickness equal to 16 times the average grain-size of the deformed material. In the case of near-surface disaggregation bands, the mineralogy is unimportant<sup>41</sup>, thus rheological control on band formation is minimal.

We emphasize that disaggregation bands can also form by non-tectonic processes, such as slumping<sup>16</sup>, and that great care must be taken to distinguish these from disaggregation bands caused by tectonic activity. Key to this is the observation of a sufficiently large number of deformation bands and that these bands form laterally and vertically extensive arrays with a constant and common strike. In contrast, bands that developed, e.g., in sediments that were deformed by an advancing ice sheet, often show a spread in strike direction<sup>42</sup>. If disaggregation bands are fault-related, the bands' orientation will show characteristic patterns with a systematic relationship to the orientation of the principle stress directions and the underlying blind fault (Fig. 1). For high differential stress/effective mean stress ( $Q/P$ ) ratios, the bands are oblique to the maximum stress direction<sup>43</sup>. Shear band orientation in unconsolidated material is grain-size dependent; in coarse sand, bands show the Roscoe orientation,  $\theta_R$ , and in fine sand, the Coulomb orientation,  $\theta_C$ <sup>44</sup>. This is in good agreement with the systematic orientation of the disaggregation bands that we observed in the analysed outcrops, where their strike closely matches that of the underlying blind faults.

Hitherto deformation bands developed in unconsolidated sediments have only been attributed to seismogenic movement on underlying faults. However, our experiments prove that disaggregation bands can also form at the typical velocities of creeping faults. This opens a new avenue of interpretation of such structures in the field. If a blind fault is creeping but not rupturing, it does not produce common indicators such as soft-sediment deformation structure (e.g., sand volcanoes), but can still cause disaggregation bands to form. From the age of the sediments in which the bands are developed, the minimum age of the blind fault activity can be derived.

We propose that the disaggregation bands form in the process zone (the area in front of the fault tip that contains all fault propagation-related deformation features of a propagating blind fault (Fig. 7)). A model that demonstrates the fracture distribution and orientation around the tip of a fault was shown by<sup>45</sup>. According to<sup>46</sup>, the size of the process zone scales rather with the size of an active slipping patch on the fault and not the total length of the fault. We postulate that the disaggregation bands shown in this study are analogue to these fractures. The

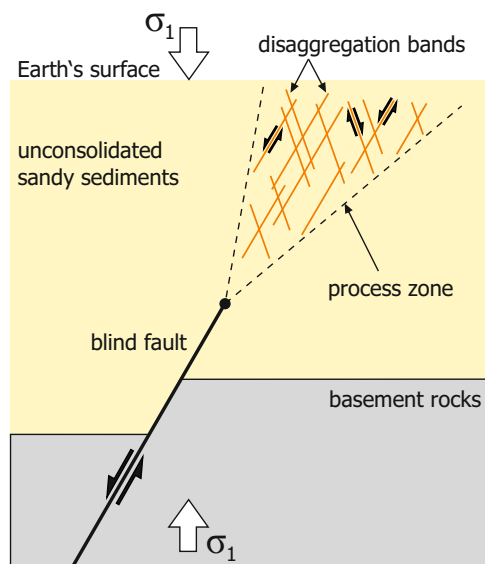


**Fig. 7 Conceptual model for the disaggregation band formation, based on<sup>47</sup>.** The bands develop in the process zone of a blind fault. For this reason, they are a suitable indicator of paleo-fault activity, even if the fault does not reach the Earth's surface.

development of disaggregation bands above blind faults is therefore a common process in sandy, unconsolidated media<sup>47</sup>. In our opinion, there is the need to further investigate disaggregation bands, both in the field and in experimental studies.

## Conclusions

We demonstrate that disaggregation bands can form in a sandy medium in the process zone of an active creeping fault. We suggest their tabular geometry results from strain hardening that forces the bands to grow thicker. The fact that they can form at very low shear velocities, typical of creeping faults, makes them a suitable indicator of slow slip on faults that do not rupture and thus do not emit seismic energy. Disaggregation bands can fill the gap left by structures that form co-seismically due to groundwater-expulsion driven by seismic energy (e.g., sand-volcanoes and clastic dykes), but fail to indicate creep activity. Disaggregation bands are thus key structures that record large parts of the seismic cycle. As such, they are a very powerful, universal indicator that are easily recognisable in natural outcrops and artificial trenches.

## Methods

**Fieldwork and sampling.** The structural datasets were measured with a standard Freiberg compass and visualised as stereographic projections. Prior to the measurements, the outcrop face perpendicular to the strike of the disaggregation bands was cleaned with a trowel. The disaggregation bands were sampled using metal cylinders with a diameter of 7 cm and a depth of 5 cm. The samples were first dried and then conserved with epoxy resin (Araldite® 2020, Huntsman). The resin was dyed blue to better visualise pore-space. Subsequently the samples were cut with a rock saw and thin-sections were made. The host material was also sampled for grain-size analysis. Material that was used for the experiments was taken from the same location.

**Grain-size analysis.** For grain-size analysis, 2.5 kg material was dried. The grain-size distribution of the material was analysed with standard grain-size sieves (DIN 4188, Retsch GmbH & Co KG and DIN ISO 3310-1, Haver & Boecker). The weight of the material after each sieve size was determined with scales (Mettler Toledo Classic PB 153-S and Mettler Toledo New Classic MF, accurate to 1 and 10 mg, respectively). Subsequently, the sieve data were analysed using the GRADISTAT program<sup>48</sup>.

**Table 1 Values used to calculate the sand material parameters.**

	Units	Value
Quartz density <sup>56</sup>	kg m <sup>-3</sup>	2650.0
Porosity <sup>57</sup>	%	36.0
Bulk density of sand	kg m <sup>-3</sup>	1696.0
Gravity	m s <sup>-2</sup>	9.81
Diameter of upper tube	m	0.045
Area of shear	m <sup>2</sup>	0.00159

**Table 2 Sand material parameters.**

	Units	Median	1 $\sigma$
Coefficient of determination ( $R^2$ )		0.994	0.004
Cohesive strength ( $\gamma$ -intercept, $C_0$ )	Pa	75.384	17.691
Coefficient of friction		0.642	0.037
Angle of internal friction ( $\mu$ )	°	32.67	1.50

**Experiments.** The shear experiments were carried out in a box with the dimensions — 30 cm length, 20 cm width and 4 cm depth. The box consists of two halves, one half is fixed and the other half is moved by an electric motor. The motor is powered with direct current and the speed can be regulated. The maximum offset that can be achieved is 6 cm (Fig. 4). We used this setup because it is well established and was successfully applied for analogue experiments to model geometrical features in shear zones<sup>32</sup>. The experiments were conducted using the original sediment from the field, and hence no upscaling is necessary, as the resulting structures are the same size as the field examples. The sand was dried before the experiments and carefully sprinkled into the shear box from a height of 2 cm. The experiments were carried out at two different shear-velocities (2 and 3600 cm h<sup>-1</sup>), at an ambient temperature of 17 °C and a humidity of 54–55%. The evolving shear band in the centre of the box was conserved with blue-dyed resin (Araldite® 2020, Huntsman) that was dripped on to the surface of the model and subsequently percolated into the sand. After each experiment, the box was emptied and cleaned. The moving half of the box was brought back into the initial position and the box was then refilled with new sand.

The material properties of the sand (angle of internal friction ( $\mu$ ) and cohesive strength ( $C$ )) that was used for the experiments were derived using a Hubbert-type shear apparatus. The shear apparatus is based on the set-up of<sup>49</sup>, which consists of two tubes. In our setup, the tubes have 4.5 cm inner diameter. The upper tube is suspended above the fixed lower tube with a gap of 0.3 mm that defines the future fault. The normal load is given by the height of the sand pile in the upper tube ( $h$ ), which was increased from 1 to 6 cm in increments of 1 cm. Similar to the experiments of<sup>49</sup>, the sand was filled in the upper tube by carefully pouring from a constant height. The shear load is applied by filling a sand-filled plastic cup that is connected via a pulley to the upper tube. The cup was loaded until the upper tube moved. The mass of the cup ( $m$ ) was measured with an electronic scales. The normal stress ( $\sigma_n$ ) and the shear stress ( $\tau$ ) were calculated with the following formulas:

$$\sigma_n = \rho gh \quad \text{and} \quad \tau = \frac{mg}{A}$$

where  $\rho$  is the density of the sand,  $g$  is the acceleration due to gravity, and  $A$  is the area of the sheared surface (see Table 1). Each experiment was run three times. By plotting shear stress vs. normal stress, we determine the slope of the curve, which gives the angle of internal friction ( $\mu$ ), and the  $y$ -intercept of the curve delivers the cohesion ( $C$ ) of the sand (see Table 2).

**$\mu$ -CT imaging.** The 3-D imaging was performed using a high-resolution, X-ray computed tomography ( $\mu$ -CT) system (nanotom® 180S, Baker Hughes, formerly part of GE Sensing & Inspection Technologies), equipped with a special water-cooled, nanofocus X-ray tube (180 kV, 15 W). For this study, bar-shaped samples with a length of 8 cm and a square cross-section of 1 cm<sup>2</sup> were cut from the larger cores, so that a voxel resolution of 9  $\mu$ m was achieved. More details on the scanning procedure can be found in<sup>50</sup>. After sample scanning, the 3-D image was reconstructed, and noise and artifacts (e.g., ring artifacts and beam hardening) were reduced. For the scans used in this study, a non-local means filter<sup>51</sup> was applied (settings: search radius 21, local neighbourhood 5, similarity 0.6). After filtering, the grains and the pores were segmented and separated from each other. This was carried out by manually cross-checking the segmentation threshold image with the according, i.e., original, grey-value image. This was followed by a slice-by-slice pore volume calculation. Individual pores were separated from each other using

watershed algorithms<sup>52</sup>. For all data sets, digital volumes of about 2–2.5 cm<sup>3</sup> were investigated. The individual geometric analysis was performed according to described procedures<sup>53–55</sup>. All of the presented data and results are derived by using the AVIZO™ toolbox (version 9.5.0) from Thermo Fischer Scientific.

## Data availability

All our analyses are available via figshare. Grainsize analysis— <https://doi.org/10.6084/m9.figshare.19291595.v1>, <https://doi.org/10.6084/m9.figshare.19291670.v1> Grain orientation— <https://doi.org/10.6084/m9.figshare.19291661.v1> Hubbert shear-box results — <https://doi.org/10.6084/m9.figshare.19291604.v1>.

Received: 16 September 2020; Accepted: 24 March 2022;

Published online: 26 April 2022

## References

- Quigley, M. C. et al. The 2010–2011 Canterbury Earthquake Sequence: environmental effects, seismic triggering thresholds and geologic legacy. *Tectonophysics* **672–673**, 228–274 (2016).
- Tuttle, M. P. & Schweig, E. S. Recognizing and dating prehistoric liquefaction features: lessons learned in the New Madrid seismic zone, central United States. *J. Geophys. Res.* **101**, 6171–6178 (1996).
- Tuttle, M. P. et al. The earthquake potential of the New Madrid Seismic Zone. *Bull. Seis. Soc. Am.* **92**, 2080–2089 (2002).
- Holzer, T. L. & Clark, M. M. Sand boils without earthquakes. *Geology* **21**, 873–876 (1993).
- Bertran, P., Font, M., Giret, A., Manchuel, K. & Sicilia, D. Experimental soft-sediment deformation caused by fluidization and intrusive ice melt in sand. *Sedimentology* **66**, 1102–1117 (2019).
- Sibson, R. H. Earthquake faulting as a structural process. *J. Struct. Geol.* **11**, 1–14 (1989).
- Kaprov, B. M. & Marone, C. Slow earthquakes, preseismic velocity changes, and the origin of slow frictional stick-slip. *Science* **341**, 1229–1232 (2013).
- Harris, R. A. Large earthquakes and creeping faults. *Rev. Geophys.* **55**, 169–198 (2017).
- Cohn, S. N., Allen, C. R., Gilman, R. & Gouly, N. R. Preearthquake and postearthquake creep on the Imperial fault and the Brawley fault zone In *The Imperial Valley, California, Earthquake of October 15, 1979. U.S. Geol. Surv. Prof. Pap.* **1254**, 161–167 (1982).
- Peng, Z. & Gomberg, J. An integrated perspective of the continuum between earthquakes and slow-slip phenomena. *Nature Geosci.* **3**, 599–607 (2010).
- Ferrelli, L., Michetti, A. M., Serva, L. & Vittori, E. Stratigraphic evidence of coseismic faulting and aseismic fault creep from exploratory trenches at Mt. Etna Volcano (Sicily, Italy) In *Ancient seismites* (eds. Etnensohn, F. R., Rest, N. & Brett, C. E.) Sp. Paper 359, 49–62 (Geological Society of America, 2002).
- Aydin, A. Small faults formed as deformation bands in sandstone. *Pure Appl. Geophys.* **116**, 913–930 (1978).
- Fossen, H., Schultz, R. A., Shipton, Z. K. & Mair, K. Deformation bands in sandstone: a review. *J. Geol. Soc. London* **164**, 755–769 (2007).
- Hesthammer, J. & Fossen, H. Structural core analysis from the Gullfaks area, northern North Sea. *Mar. Petrol. Geol.* **18**, 411–439 (2001).
- Shipton, Z. K., Evans, J. P. & Thompson, L. B. The geometry and thickness of deformation-band fault core and its influence on sealing characteristics of deformation-band fault zones. In *Faults, fluid flow, and petroleum traps* (eds. Sorkhabi, R. & Tsuji, Y.) AAPG Memoir 85, 181–195 (2005).
- Fossen, H. Deformation bands formed during soft-sediment deformation: observations from SE Utah. *Mar. Petrol. Geol.* **27**, 215–222 (2010).
- Cashman, S. M., Baldwin, J. N., Cashman, K. V., Swanson, K. & Crawford, R. Microstructures developed by coseismic and aseismic faulting in near-surface sediments, San Andreas Fault, California. *Geology* **35**, 611–614 (2007).
- Shipton, Z. K., Meghraoui, M. & Monro, L. Seismic slip on the west flank of the Upper Rhine Graben (France-Germany): evidence from tectonic morphology and cataclastic deformation bands. In *Seismicity, fault rupture and earthquake hazards in slowly deforming regions* (eds. Landgraf, A., Kuebler, S., Hintersberger, E. & Stein, S.) *Geol. Soc., London, Sp. Publ.* **432**, 147–161 (2017).
- Rawling, G. C. & Goodwin, L. B. Cataclasis and particulate flow in faulted, poorly lithified sediments. *J. Struct. Geol.* **25**, 317–331 (2003).
- Wolf, H., König, D. & Triantafyllidis, T. Experimental investigation of shear band patterns in granular material. *J. Struct. Geol.* **25**, 1229–1240 (2003).
- Mair, K., Main, I. & Elphick, S. Sequential growth of deformation bands in the laboratory. *J. Struct. Geol.* **22**, 25–42 (2000).

22. Brandes, C., Steffen, H., Sandersen, P. B. E., Wu, P. & Winsemann, J. Glacially induced faulting along the NW segment of the Sorgenfrei-Tornquist Zone, northern Denmark: implications for neotectonics and Lateglacial fault-bound basin formation. *Quat. Sci. Rev.* **189**, 149–168 (2018).
23. Gregersen, S., Glendrup, M., Larsen, T. B., Voss, P. & Rasmussen, H. P. Seismology: neotectonics and structure of the Baltic shield. *Geol. Surv. Den. Grenl. Bull.* **7**, 25–28 (2005).
24. Veldkamp, A., Van den Berg, M. W., Van Dijke, J. J. & Van den Berg van Saparoea, R. M. Reconstructing Late Quaternary fluvial process controls in the upper Aller Valley (North Germany) by means of numerical modeling. *Neth. J. Geosci.* **81**, 375–388 (2002).
25. Leydecker, G. Erdbebenkatalog für Deutschland mit Randgebieten für die Jahre 800 bis 2008. (Earthquake catalogue for Germany and adjacent areas for the years 800 to 2008). *Geologisches Jahrbuch E* **59**, 1–198 (2011).
26. Brandes, C. et al. Visualisation and analysis of shear-deformation bands in unconsolidated Pleistocene sand using ground-penetrating radar: implications for paleoseismological studies. *Sediment. Geol.* **367**, 135–145 (2018).
27. Winsemann, J. et al. Ice-marginal forced regressive deltas in glacial lake basins: geomorphology, facies variability and large-scale depositional architecture. *Boreas* **47**, 973–1002 (2018).
28. Kristensen, M. B., Childs, C., Olesen, N. Ø. & Korstgård, J. A. The microstructure and internal architecture of shear bands in sand-clay sequences. *J. Struct. Geol.* **46**, 129–141 (2013).
29. Wei, M., Kaneko, Y., Liu, Y. & McGuire, J. J. Episodic fault creep events in California controlled by shallow frictional heterogeneity. *Nature Geosci.* **6**, 566–570 (2013).
30. Doglioni, C., Barba, S., Carminati, E. & Riguzzi, F. Fault on-off versus strain rate and earthquakes energy. *Geosci. Front.* **6**, 265–276 (2015).
31. Lyons, S. & Sandwell, D. Fault creep along the southern San Andreas from interferometric synthetic aperture radar, permanent scatterers, and stacking. *J. Geophys. Res.* **108/B1**, 2047 (2003).
32. Schrank, C. E., Boutelier, D. A. & Cruden, A. R. The analogue shear zone: From rheology to associated geometry. *J. Struct. Geol.* **30**, 177–193 (2008).
33. Ritter, M. C., Rosenau, M. & Onno, O. Growing faults in the lab: Insights into the scale dependence of the fault zone evolution process. *Tectonics* **37**, 140–153 (2018).
34. Vardoulakis, I. G. & Sulem, J. *Bifurcation analysis in geomechanics*. (Taylor & Francis, 1995).
35. Schultz, R. A. & Siddharthan, R. A general framework for the occurrence and faulting of deformation bands in porous granular rocks. *Tectonophysics* **411**, 1–18 (2005).
36. Collins, I. F., Muhunthan, B., Tai, A. T. T. & Pender, M. J. The concept of a ‘Reynolds-Taylor’ state and the mechanics of sands. *Géotechnique* **57**, 437–447 (2007).
37. Sawicki, A. Dilation and modelling of sands in the light of experimental data. *Arch. Hydroengineering Environ. Mech.* **61**, 3–15 (2014).
38. Wegner, S. et al. Effects of grain shape on packing and dilatancy of sheared granular material. *Soft Matter* **10**, 5157–5167 (2014).
39. Oda, M. & Kazama, H. Microstructure of shear bands and its relation to the mechanisms of dilatancy and failure of dense granular soils. *Géotechnique* **48**, 465–481 (1998).
40. Mühlhaus, H.-B. & Vardoulakis, I. The thickness of shear bands in granular materials. *Géotechnique* **37**, 271–283 (1987).
41. Beke, B., Fodor, L., Millar, L. & Petrik, A. Deformation band formation as a function of progressive burial: Depth calibration and mechanism change in the Pannonian Basin (Hungary). *Mar. Pet. Geol.* **105**, 1–16 (2019).
42. Müller, K. et al. The challenge to distinguish soft-sediment deformation structures (ssds) formed by glaciotectionic, periglacial and seismic processes in a formerly glaciated area. In *Glacially-Triggered Faulting* (eds Steffen, H., Olesen, O. & Sutinen, R.) 67–88 (Cambridge University Press, 2021). <https://doi.org/10.1017/9781108779906.007>
43. Robert, R., Souloumiac, P., Robion, P. & David, C. Numerical simulation of deformation band occurrence and the associated stress field during the growth of a fault-propagation fold. *Geosciences* **9**, 257 (2019).
44. Vermeer, P. A. The orientation of shear bands in biaxial tests. *Géotechnique* **40**, 223–236 (1990).
45. Vermilye, J. M. & Scholz, C. H. The process zone: a microstructural view of fault growth. *J. Geophys. Res.* **103**, 12223–12237 (1998).
46. Cowie, P. A. & Shipton, Z. K. Fault tip displacement gradients and process zone dimensions. *J. Struct. Geol.* **20**, 983–997 (1998).
47. Ballas, G., Fossen, H. & Soliva, R. Factors controlling permeability of cataclastic deformation bands and faults in porous sandstone reservoirs. *J. Struct. Geol.* **76**, 1–21 (2015).
48. Blott, S. J. & Pye, K. GRADISTAT: a grain size distribution and statistics package for the analysis of unconsolidated sediments. *Earth Surf. Process. Landforms* **26**, 1237–1248 (2001).
49. Schellart, W. P. Shear test results for cohesion and friction coefficients for different granular materials: scaling implications for their usage in analogue modelling. *Tectonophysics* **324**, 1–16 (2000).
50. Halisch, M., Steeb, H., Henkel, S. & Krawczyk, C. M. Pore-scale tomography and imaging: applications, techniques and recommended practice. *Solid Earth* **7**, 1141–1143 (2016).
51. Shreyamsha Kumar, B. K. Image denoising based on non-local means filter and its method noise thresholding. *Signal Image Video Processing* **7**, 1211–1227 (2013).
52. Soille, P. *Morphological image analysis: principles and applications* (Springer, 2003). <https://doi.org/10.1007/978-3-662-05088-0>
53. Schmitt, M., Halisch, M., Müller, C. & Fernandes, C. P. Classification and quantification of pore shapes in sandstone reservoir rocks with 3-D X-ray micro-computed tomography. *Solid Earth* **7**, 285–300 (2016).
54. Halisch, M., Schmitt, M. & Fernandes, C. P. Pore shapes and pore geometry of reservoir rocks from  $\mu$ -CT imaging and digital image analysis. In *Proceedings of Society of Core Analysts (SCA) Annual Meeting 2016*, Snowmass, Colorado, USA, SCA2016-093 (2016).
55. Halisch, M., Schmitt, M., Kruschwitz, S. & Weller, A. Quantification of rock structures with high resolution X-ray  $\mu$ -CT for laboratory SIP measurements. In *4th International Workshop on Induced Polarization*, Aarhus, Denmark, (2016).
56. Deer, W. A., Howie, R. A. & Zussman, J. *An introduction to the rock-forming minerals*. 340–355 (Wiley, 1966).
57. Curry, C. W. et al. Comparative study of sand porosity and a technique for determining porosity of undisturbed marine sediment. *Mar. Georesources Geotechnol.* **22**, 231–252 (2010).
58. Kley, J. & Voigt, T. Late Cretaceous intraplate thrusting in central Europe: effect of Africa-Iberia-Europe convergence, not Alpine collision. *Geology* **36**, 839–842 (2008).
59. Müller, K. et al. Glacially-induced faults in Germany. In *Glacially-triggered faulting* (eds Steffen, H., Olesen, O. & Sutinen, R.) 283–303 (Cambridge University Press, 2021). <https://doi.org/10.1017/9781108779906.021>
60. Vollmer, F. W. Automatic contouring of geologic fabric and finite strain data on the unit hyperboloid. *Comput. Geosci.* **115**, 134–142 (2018).

## Acknowledgements

We are grateful to Peter Blisniuk (Stanford University) and Jutta Winsemann (Leibniz Universität Hannover) for discussions on this subject. Sabine Mogwitz (LAG) weighed the sieve samples. We thank Juliet G. Crider, Jess McBeck and an anonymous reviewer for thorough and constructive reviews to the manuscript. We thank the owner of the Ulrich sand-pit, Freden for access to their property and permission to sample the sand.

## Author contributions

C.B. designed the study, carried out fieldwork, conducted the experiments and contributed to the thin-section analysis. D.C.T. contributed to the fieldwork, carried out the statistical analysis and contributed to the thin-section analysis. M.H. carried out  $\mu$ -CT Imaging, 3-D digital image processing and analysis. H.F. contributed scientific information to the study and conducted the strain rate determination. K.M. contributed to the fieldwork, prepared the samples and contributed to the thin-section analysis. All authors contributed to the writing and finalisation of the manuscript.

## Funding

Open Access funding enabled and organized by Projekt DEAL.

## Competing interests

The authors declare no competing interests.

## Additional information

**Supplementary information** The online version contains supplementary material available at <https://doi.org/10.1038/s43247-022-00423-8>.

**Correspondence** and requests for materials should be addressed to Christian Brandes.

**Peer review information** Communications Earth & Environment thanks Juliet Crider, Jessica McBeck and the other, anonymous, reviewer(s) for their contribution to the peer review of this work. Primary Handling Editor: Joe Aslin. Peer reviewer reports are available.

**Reprints and permission information** is available at <http://www.nature.com/reprints>

**Publisher's note** Springer Nature remains neutral with regard to jurisdictional claims in published maps and institutional affiliations.



**Open Access** This article is licensed under a Creative Commons Attribution 4.0 International License, which permits use, sharing, adaptation, distribution and reproduction in any medium or format, as long as you give appropriate credit to the original author(s) and the source, provide a link to the Creative Commons license, and indicate if changes were made. The images or other third party material in this article are included in the article's Creative Commons license, unless indicated otherwise in a credit line to the material. If material is not included in the article's Creative Commons license and your intended use is not permitted by statutory regulation or exceeds the permitted use, you will need to obtain permission directly from the copyright holder. To view a copy of this license, visit <http://creativecommons.org/licenses/by/4.0/>.

© The Author(s) 2022